Supporting Information

Defect engineering of NiCo-layered double hydroxide hollow nanocage for highly selective photoreduction of CO$_2$ to CH$_4$ with suppressing H$_2$ evolution

Jiamin An,[†a] Tianyang Shen,[†a] Wen Chang,[a] Yufei Zhao,[a] Bo Qi,[*a] and Yu-Fei Song[*a]

---

a   Jiamin An, Tianyang Shen, Wen Chang, Prof.Yufei Zhao, Dr. Bo Qi, and Prof.Yu-Fei Song
     Beijing Advanced Innovation Center for Soft Matter Science and Engineering, State Key
     Laboratory of Chemical Resource Engineering
     Beijing University of Chemical Technology, Beijing 100029, China.
     E-mail:bqi@mail.buct.edu.cn; songyf@mail.buct.edu.cn.

†   These authors contributed equally to this work.

Experimental Section

Materials. $Ni(NO_3)_2 \cdot 6H_2O$ (99%), $Co(NO_3)_2 \cdot 6H_2O$ (99%), Triethanolamine (TEOA), $[Ru(bpy)_3]Cl_2 \cdot 6H_2O$ (bpy = 2'2-bipyridine), 2-methylimidazole (99%), and hexamethylenetetramine (HMT) were purchased from Energy Chemical. CH_3OH, C_2H_5OH, and other used solvents (analytical grade) were purchased from Sigma-Aldrich. All materials and reagents were used directly without any further purification. Deionized water was used in all the experimental processes.

Preparation of ZIF-67 Nanoparticles. Typically, $Co(NO_3)_2 \cdot 6H_2O$ (291.0 mg ,1.0 mmol) and 2-methylimidazole (328.4 mg, 4.0 mmol) were dissolved in 25 mL methanol, respectively. Then, the latter clear solution was quickly added into the former pink solution and the resultant suspension was kept for 24 h at room temperature. The purple-colored product (about 40 mg) was obtained after centrifugation, washed with methanol, and dried at room temperature.

Synthesis of HC-NiCo-LDH. First, 40 mg as-prepared ZIF-67 nanoparticles and 200 mg $Ni(NO_3)_2 \cdot 6H_2O$ were each dissolved in 13 mL ethanol. Then, the above two solutions were mixed under magnetic stirring. Then the mixture was refluxed for 1 h under stirring. The resultant product was obtained by centrifugation, washed with ethanol several times, and dried under vacuum condition.

Preparation of Bulk-NiCo-LDH. First, 0.08 mol of $Ni(NO_3)_2 \cdot 6H_2O$ and 0.02 mol of $Co(NO_3)_2 \cdot 6H_2O$ and 0.1 mol HMT dissolved in 100 mL of deionized water. Then the resulting solution was transferred to a Teflon-lined autoclave to be heated to 95 °C for 14 h. Finally, the laurel-green precipitate was recovered by centrifuging the mixture, washing it several times with deionized water and ethanol, and then drying overnight at 70 °C in air.

Characterization. Powder X-ray diffraction (XRD) patterns of the samples were collected on a Rigaku XRD-6000 diffractometer equipped with a Cu Kα radiation (λ =

1.5405 Å). The morphology and microstructure of all samples were observed using a high-resolution transmission electron microscopy (HRTEM, JEOL JEM-2010) and a scanning electron microscopy (SEM, Zeiss Supra55). Inductively coupled plasma spectroscopy (ICP-MS) analyses were carried out on a Shimadzu ICPS-7500 spectrometer to further confirm the relative molar ratio of the metal in the bimetallic LDH. Brunauer-Emmett-Teller (BET) surface areas were determined using N_2 adsorption-desorption isotherms measured on a Quanta chrome Autosorb-1C analyzer. Fourier transform infrared (FT-IR) spectra were recorded on a Perkin Elmer FT-IR spectrophotometer to get the fingerprint of the chemical bonding vibration of the material. Surface composition and valence state of metal elements were analyzed by the X-ray photoelectron spectroscopy (XPS, ESCALAB250) instrument, equipped with a 150 W Al-Kαradiations. The photoluminescence (PL) spectra were performed on a spectrophotometer (F–7000 FL) to investigate the charge recombination rate at room temperature. Solid-state UV-visible diffuse reflectance spectroscopy (DRS) were recorded on a Beijing PGENERAL TU-1901 spectrometer within a wavelength range of 200–800 nm at room temperature. Electron spin resonance (ESR) spectra were recorded on an EMX-500 10/12 ESR spectrometer. The electrochemical impedance spectroscopy (EIS) measurements and Mott-Schottky plots were performed on an electrochemical workstation (CHI 760E, China) in the presence of Na_2SO_4 (100 mM, pH = 7.0). The working electrode was prepared on fluorine-doped tin oxide (ITO) glass.
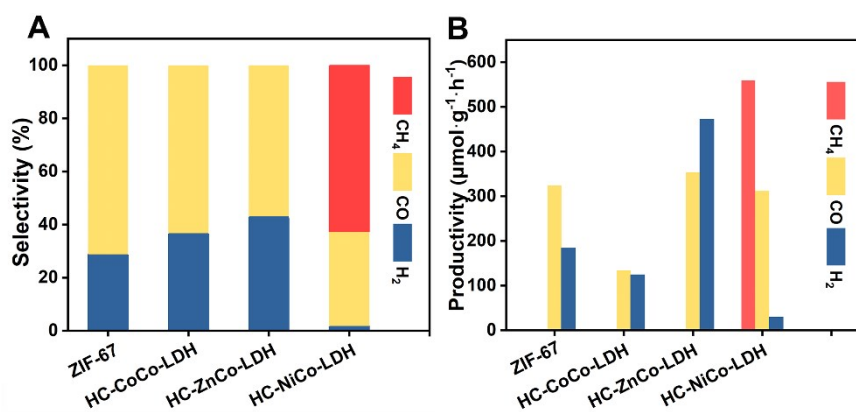
Fig. S1 (A) Selectivity and (B) Production rate of CH_4, CO, and H_2 in photocatalytic CO_2 reduction on the different catalysts.
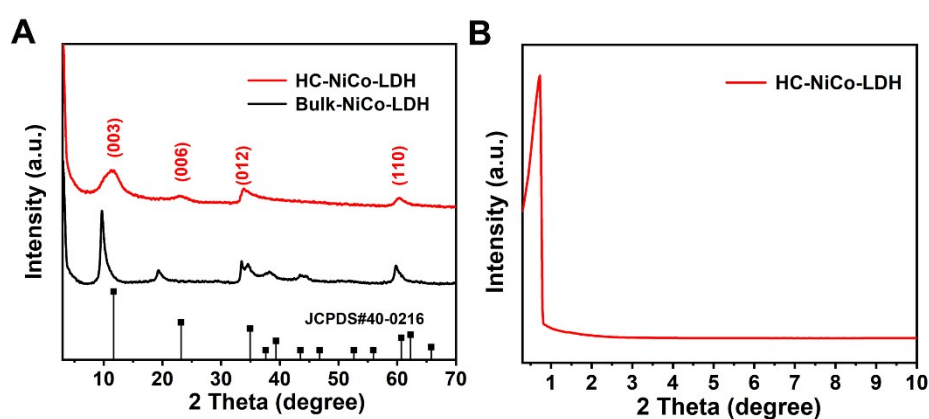
Fig. S2 (A) X-ray diffraction patterns of HC-NiCo-LDH and Bulk-NiCo-LDH, respectively, and (B) Small Angle X-ray diffraction of HC-NiCo-LDH.

Table S1 Summary of elemental analyses data for HC-NiCo-LDH and Bulk-NiCo-LDH, from ICP results

Sample	Ni/Co
HC-NiCo-LDH	3.69
Bulk-NiCo-LDH	4.12
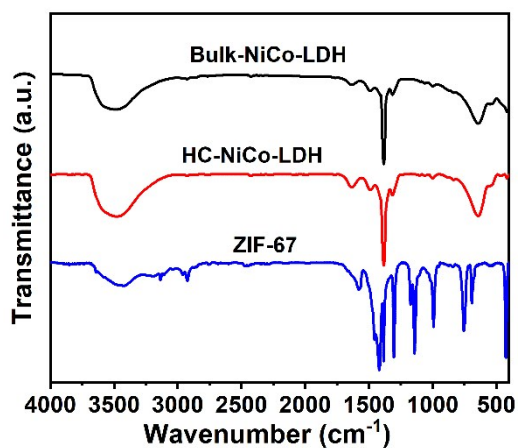
Fig. S3 FT-IR spectra of ZIF-67, HC-NiCo-LDH, and Bulk-NiCo-LDH, respectively.

As shown in Fig. S3, the FT-IR spectra of HC-NiCo-LDH and Bulk-NiCo-LDH were similar, the broadband at 3430 cm^{-1} corresponds to the mode of stretching vibration and bending vibration of the O-H bond. The smaller shoulder peak at 1630 cm^{-1} was designated to interlayer water. The peak at 1380 cm^{-1} signified the vibrations of interlayer anion and below 900 cm^{-1} belonged to the M-O and M-OH.
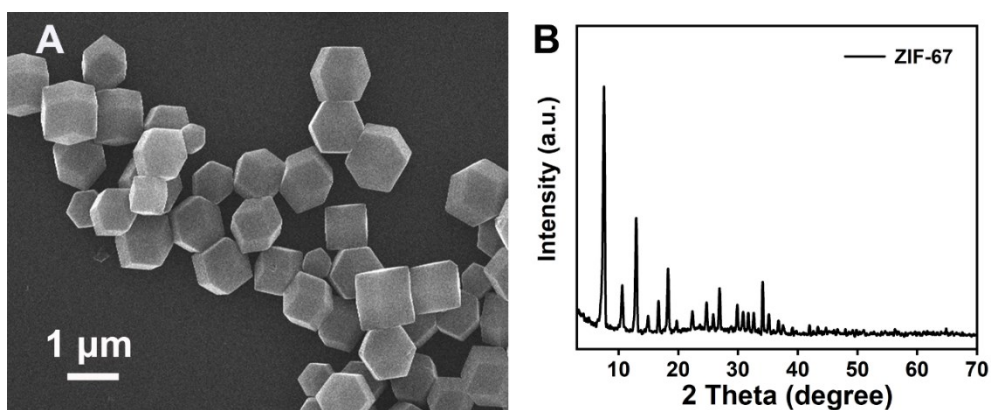
Fig. S4 (A) SEM images and (B) X-ray diffraction patterns of ZIF-67.
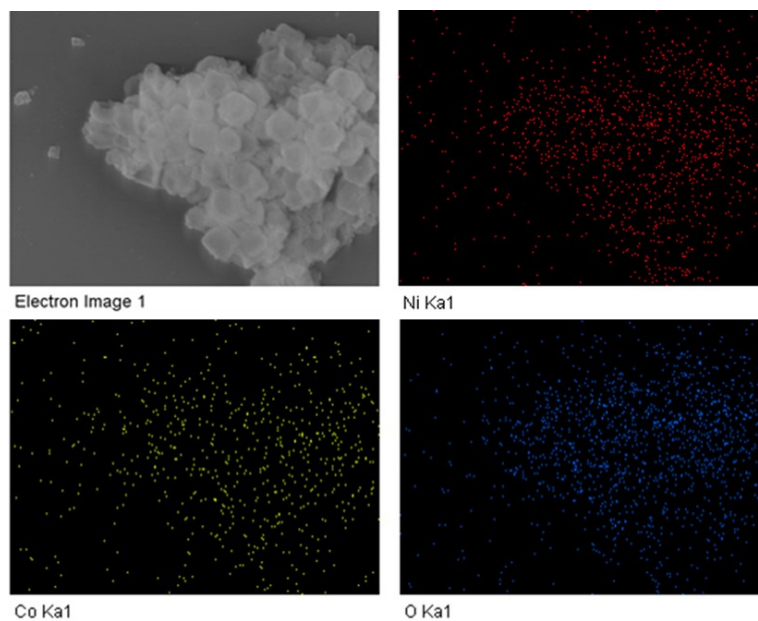
Fig. S5 SEM and elemental mapping images of HC-NiCo-LDH.
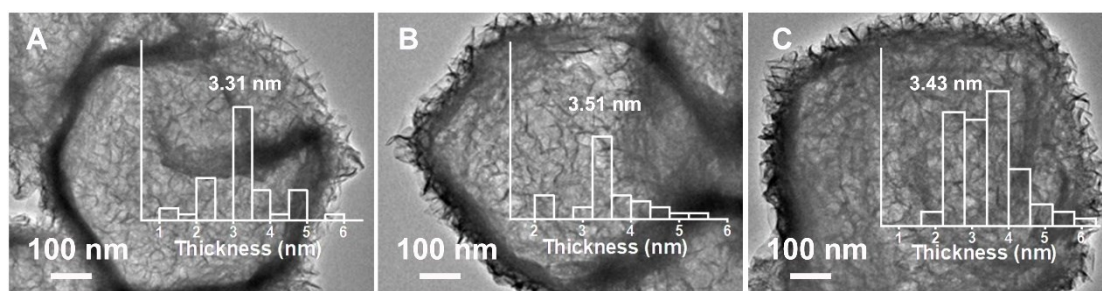
Fig. S6 HRTEM images of HC-NiCo-LDH. The insets showed the statistics of LDH thickness distribution.
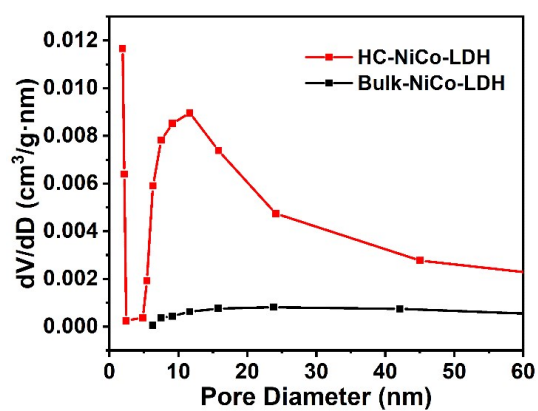
Fig. S7 Size distribution curves of HC-NiCo-LDH and Bulk-NiCo-LDH.
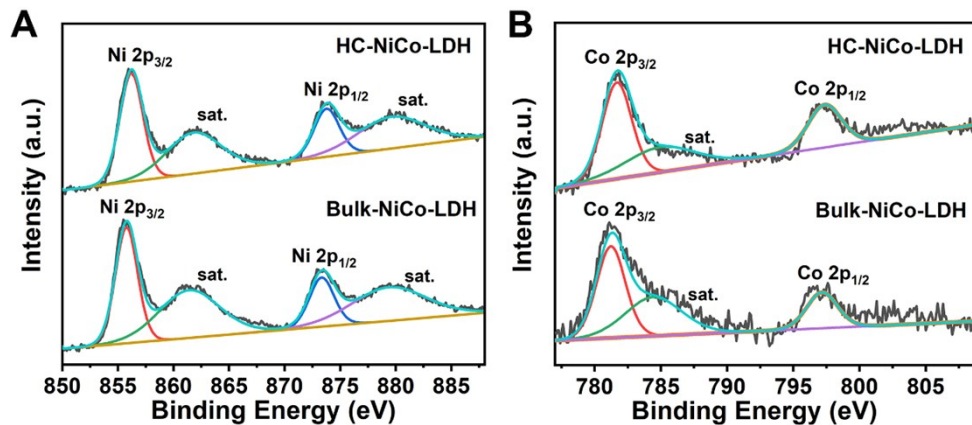
Fig. S8 High-resolution XPS spectra of (A) Ni 2p and (B) Co 2p of HC-NiCo-LDH and Bulk-NiCo-LDH, respectively.
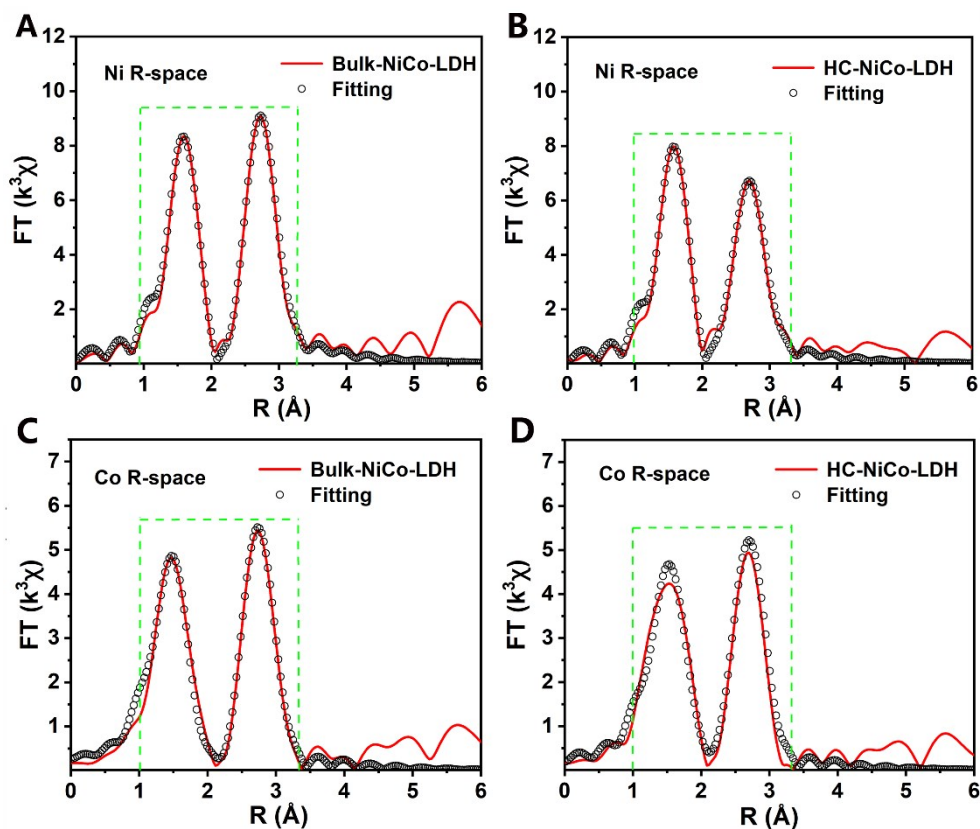
Fig. S9 Corresponding fitting of Ni K-edge XANES spectra (A, B) and Co K-edge XANES spectra (C, D) for the Bulk-NiCo-LDH and HC-NiCo-LDH, respectively.

Table S2 Local structure parameters around Ni atoms estimated by EXAFS analyses

sample	shell	N^a	R(Å)^b	δ^2 (10^{-3}Å^{-2})	S_0^2	R-factor (10^{-2})
Bulk-NiCo-LDH	Ni-O	6	2.05	5.6	1	0.57
	Ni-M (M=Ni/Co)	6	3.10	6.2		
HC-NiCo-LDH	Ni-O	5.9	2.03	5.8	1	0.85
	Ni-M (M=Ni/Co)	5.4	3.09	7.7		

Table S3 Local structure parameters around Co atoms estimated by EXAFS analyses

sample	shell	N^a	R(Å)^b	δ^2 (10^{-3}Å^{-2})	S_0^2	R-factor (10^{-2})
Bulk-NiCo-LDH	Co-O	6	1.98	6.8	1	0.87
	Co-M (M=Ni/Co)	6	3.11	10		
HC-NiCo-LDH	Co-O	5.9	2.03	8.2	1	1.92
	Co-M (M=Ni/Co)	5.6	3.05	9.8		
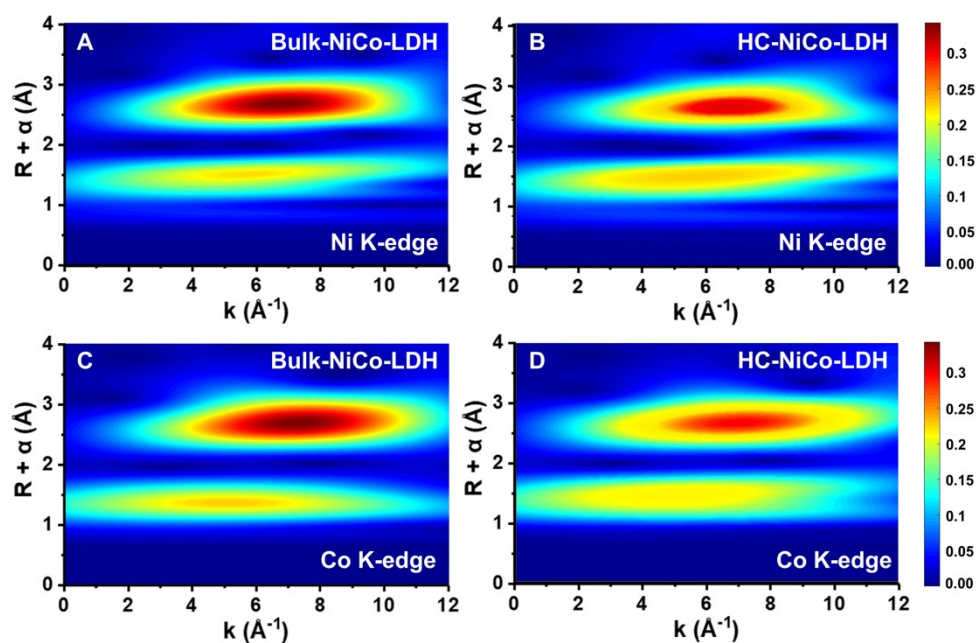
Fig. S10 WT-EXAFS of (A, B) Ni and (C, D) Co for the Bulk-NiCo-LDH and HC-NiCo-LDH, respectively.
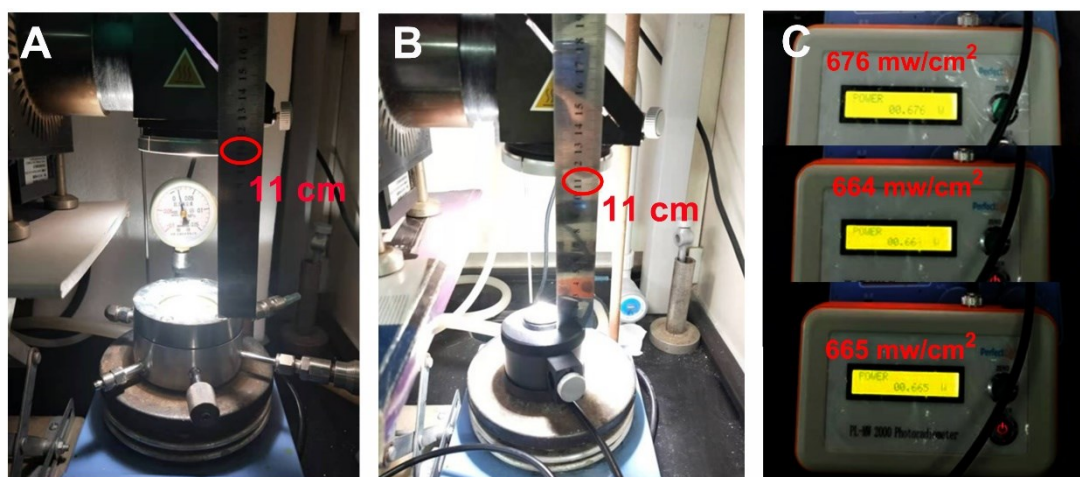
Fig. S11 (A) The photos of the reaction equipment; (B, C) The optical density value when the distance between the reaction equipment and the light was held at 11 cm.
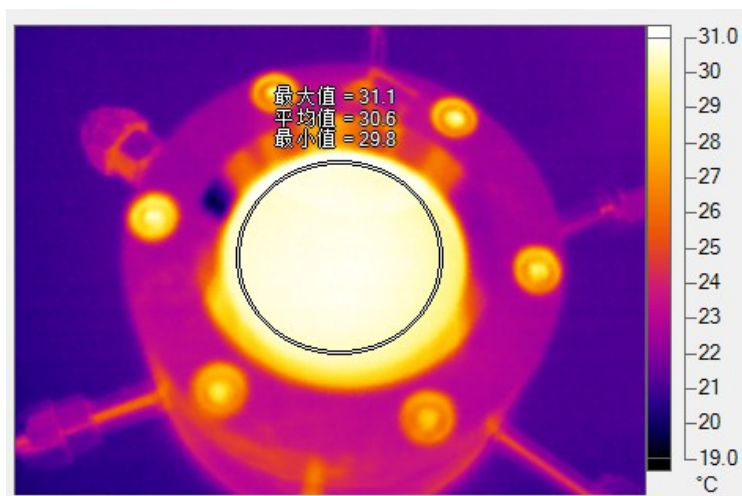
Fig. S12 The reaction temperature measured by an infrared thermal imager.
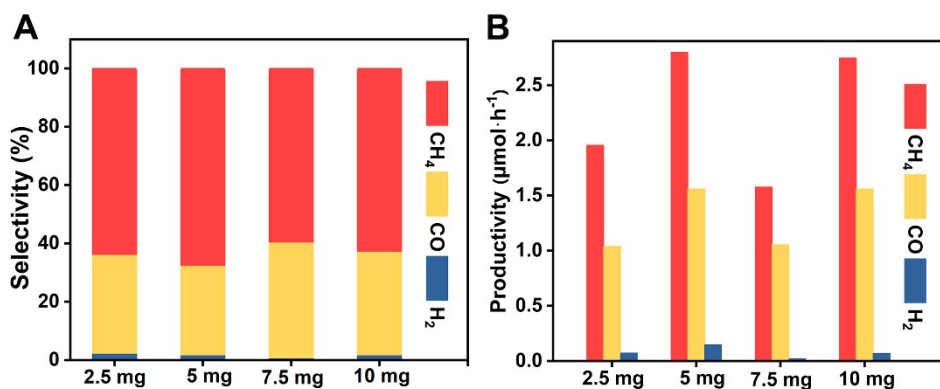
Fig. S13 (A) Selectivity and (B) Production rate of CH_4, CO, and H_2 in photocatalytic CO_2 reduction on the different amounts of HC-NiCo-LDH.

The effect of different amounts of the photocatalyst was shown in Fig. S13. The selectivity of CH_4 and H_2 exhibited little change with the increase of HC-NiCo-LDH. Therefore, 5 mg HC-NiCo-LDH was used in further CO_2 photoreduction studies to obtain higher productivity of HC-NiCo-LDH and keep a stable selectivity.
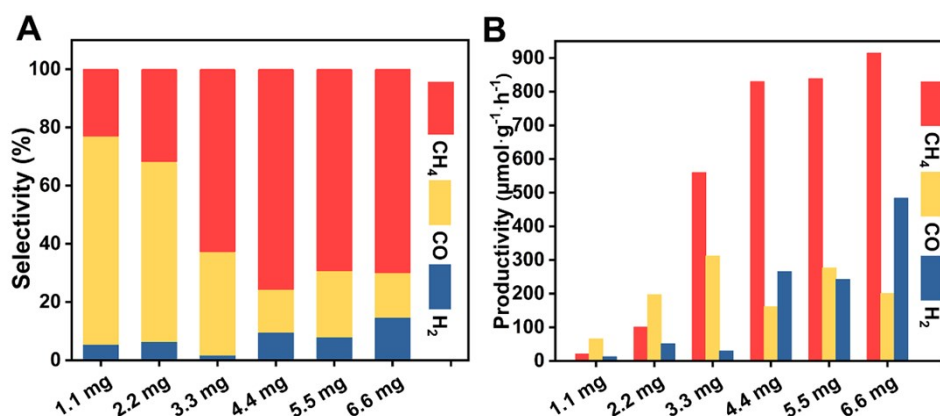
Fig. S14 (A) Selectivity and (B) Production rate of CH_4, CO, and H_2 in photocatalytic CO_2 reduction on HC-NiCo-LDH with different amounts of Ru(bpy)$_3$Cl$_2$·6H$_2$O. (irradiating with λ > 400 nm).

The effect of different concentrations Ru(bpy)$_3$Cl$_2$·6H$_2$O was shown as Fig. S14. The selectivity of CH_4 increased first with the increased concentration of Ru(bpy)$_3$Cl$_2$·6H$_2$O and then decreases after 4.4 mg, while, the selectivity of H_2 was increased with more content of Ru(bpy)$_3$Cl$_2$·6H$_2$O than 3.3 mg. Since H_2 was a by-product of this reaction, 3.3 mg Ru(bpy)$_3$Cl$_2$·6H$_2$O was better than others in the photocatalytic of CO_2. Hence, 3.3 mg Ru(bpy)$_3$Cl$_2$·6H$_2$O was add in further CO_2 photoreduction studies.
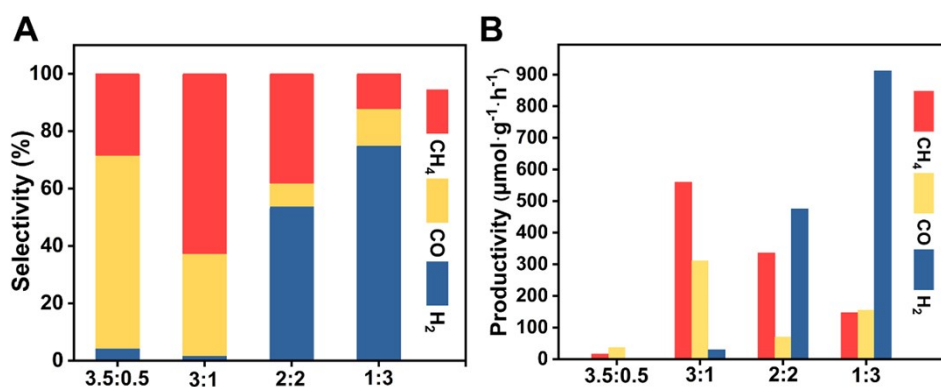
Fig. S15 (A) Selectivity and (B) Production rate of CH_4, CO, and H_2 in photocatalytic CO_2 reduction on HC-NiCo-LDH with different ratio of H_2O: TEOA (irradiating with $\lambda > 400$ nm).

A series of control experiments with a different ratio of CH_3CN: TEOA: H_2O was also conducted. It was found that 6: 1: 3 performed the highest selectivity and production rate of CH_4.

Table S4 Photocatalytic CO_2 reduction performance of different reaction system

Reaction System	selectivity (%)			yield ($\mu mol \cdot g^{-1} \cdot h^{-1}$)		
	H_2	CO	CH_4	H_2	CO	CH_4
Normal condition (Ru(bpy)$_3$Cl$_2$·6H$_2$O+HC-NiCo-LDH+TEOA)	1.77	35.57	62.66	29.5	311.92	559.54
No LDH (Ru(bpy)$_3$Cl$_2$·6H$_2$O+TEOA)	44.99	55.01	0.00	168.56	206.11	0.00
No TEOA (Ru(bpy)$_3$Cl$_2$·6H$_2$O+HC-NiCo-LDH)	0.00	0.00	0.00	0.00	0.00	0.00
No Ru(bpy)$_3$Cl$_2$·6H$_2$O (HC-NiCo-LDH+TEOA)	0.00	0.00	0.00	0.00	0.00	0.00
In dark	0.00	0.00	0.00	0.00	0.00	0.00

Normal reaction condition: photosensitizer: 4×10^{-6} mol Ru(bpy)$_3$Cl$_2$·6H$_2$O; HC-NiCo-LDH: 5 mg; solvent:10 mL (CH$_3$CN/TEOA/H$_2$O=6: 1: 3 (v/v)); $\lambda > 400$ nm, 1h.
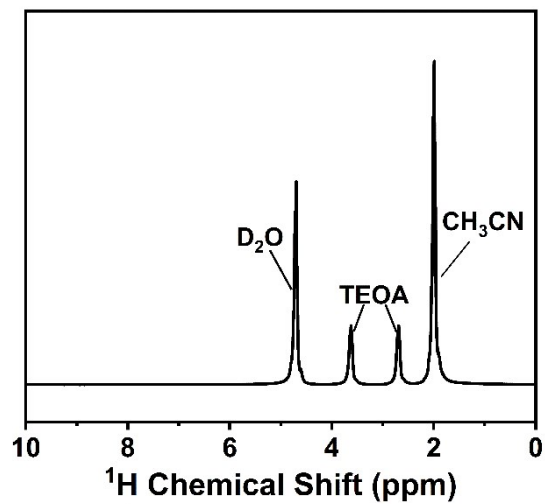
Fig. S16 ^{1}H-NMR spectra of the liquid sample taken from the reaction system (5 mg HC-NiCo-LDH after irradiation 1 h under visible light).
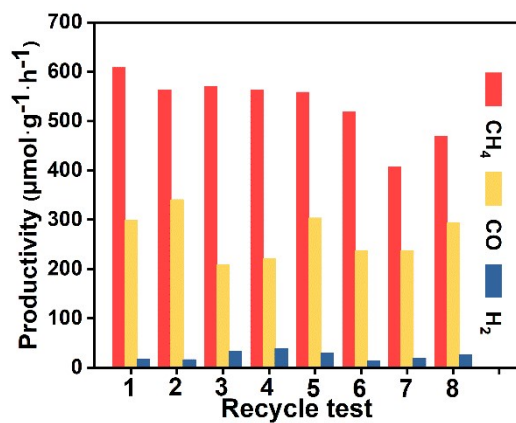
Fig. S17 Production rate of CH_4, CO, and H_2 in photocatalytic CO_2 reduction on recycled HC-NiCo-LDH (irradiating with λ > 400 nm).
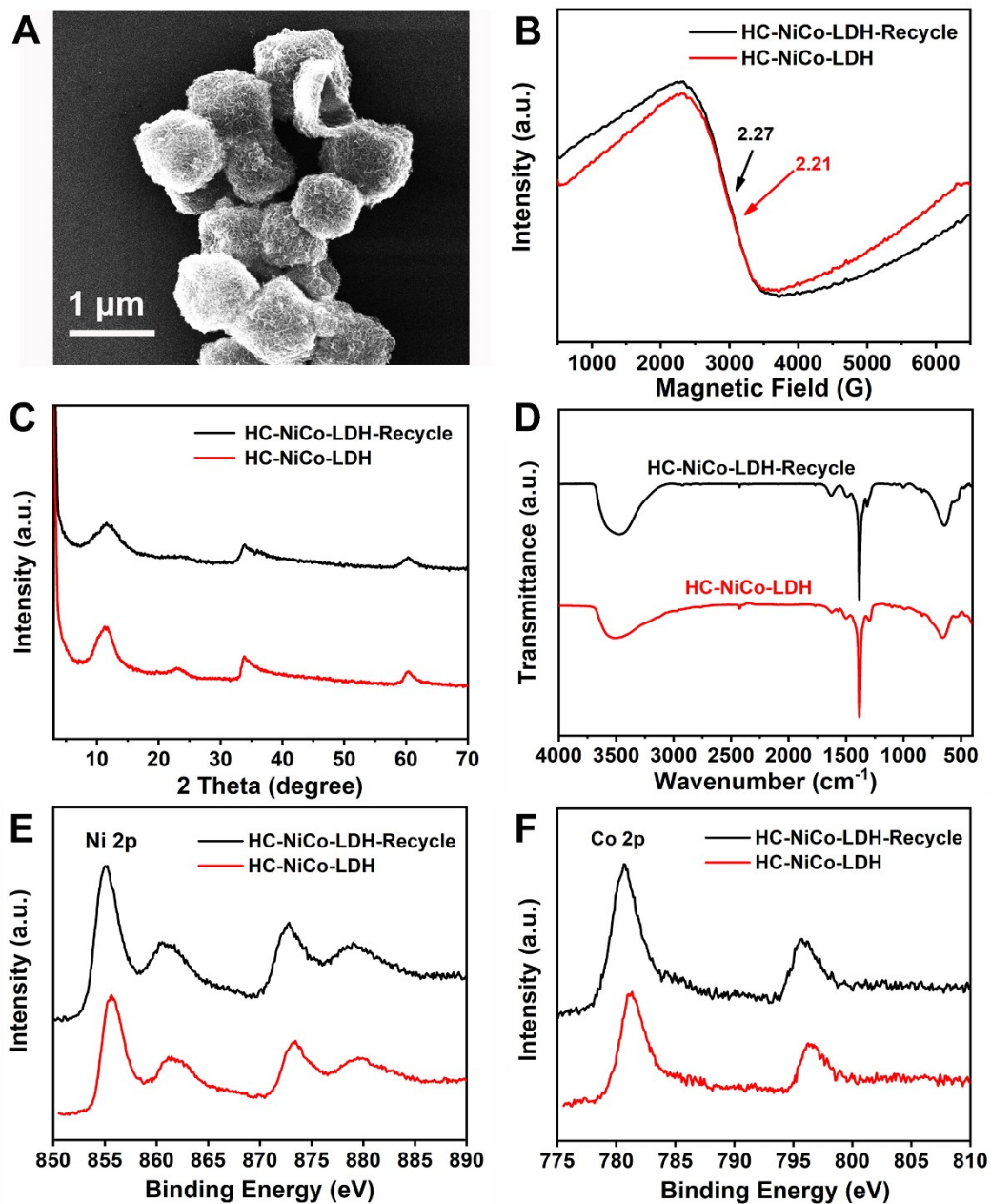
Fig. S18 The structural characterization of HC-NiAl-LDH after CO₂PR reduction test, (A) SEM images, (B) ESR spectra, (C) X-ray diffraction patterns, (D) FT-IR spectra, (E, F) XPS spectra of Ni 2p and Co 2p, respectively.

Table S5 Comparison of photocatalytic CO_2 reduction performance for various photocatalysts in this work and in previous literature

	Catalyst	Photosensitizer Co-catalyst	Sacrificial agent	Solvent	Light source	Major product selectivity	Production rate ($\mu mol \cdot g^{-1} \cdot h^{-1}$)	Reference
1	ZIF-67	[Ru(bpy)$_3$]Cl$_2$·6H$_2$O	TEOA	MeCN-H$_2$O (3: 2 v/v)	300 W Xe lamp (λ > 420 nm)	CO: 74.2% H$_2$: 25.8%	37.4($\mu mol \cdot 30min^{-1}$) 13($\mu mol \cdot 30min^{-1}$)	*Appl. Catal. B-Environ.*, 2017, 209, 476[1]
2	MOF-525-Co	-	TEOA	MeCN	300 W Xe lamp (λ = 400-800 nm)	CH$_4$: 15.5% CO: 84.5%	36.67 200.6	*Angew. Chem. Int. Ed.,* 2016, 55, 14310[2]
3	Pt/C-In$_2$O$_3$	Pt	TEOA	H$_2$O	300 W Xe	CO: 63.3% CH$_4$: 14.0% H$_2$: 22.7%	126.6($\mu mol \cdot h^{-1}$) 27.9 ($\mu mol \cdot h^{-1}$) 45.5($\mu mol \cdot h^{-1}$)	*J. Am. Chem. Soc.,* 2017, 139, 4123[3]
4	Iron tetraphenylporphyrin complex	Ir(ppy)$_3$	TEA	MeCN-H$_2$O (2: 1 v/v）	300 W Xe (λ > 420 nm)	CH$_4$: 83% H$_2$: 17%	1865 382	*Nature,* 2017, 548, 74[4]
5	Auc-C-Co	-	TEOA	MeCN	300 W Xe (λ > 420 nm)	CO: 65.2% CH$_4$: 5.7% H$_2$: 29.1%	0.075 3.451 1.539	*J. Am. Chem. Soc.,* 2018, 140, 16514[5]
6	Ni(0.26%): CdS QD	-	TEOA	H$_2$O	300 W Xe (λ > 400 nm)	CO: 88.8% CH$_4$: 11.2%	~9.5 ~1.3	*Angew. Chem. Int. Ed.,* 2018, 57, 16447[6]
7	NENU-606	[Ru(bpy)$_3$]Cl$_2$·6H$_2$O	TEOA	H$_2$O	300 W Xe (λ > 420 nm)	CO: 14.5% CH$_4$: 85.5%	0.2957 1.7478	*Chem. Sci.,* 2019, 10, 185[7]
8	QA/rGO-2	-	TEOA	H$_2$O	300 W Xe (λ > 420 nm)	CO: 60.0% CH$_4$: 36.7% H$_2$: 3.3%	450 275 24.75	*Ind. Eng. Chem. Res.* 2019, 58, 9636[8]
9	Monolayer NiAl-LDH	Ru(bpy)$_3$ Cl$_2$·6H$_2$O	TEOA	MeCN-H$_2$O (3: 1 v/v)	300 W Xe (λ > 600 nm)	CH$_4$: 70.3% CO: 29.7%	103 43	*Angew. Chem. Int. Ed.,* 2019, 58, 11860[9]
10	HC-NiCo-LDH	[Ru(bpy)$_3$]Cl$_2$·6H$_2$O	TEOA	MeCN-H$_2$O (2: 1 v/v)	300 W Xe (λ ≥ 400 nm)	CH$_4$: 62.7% CO: 35.6 % H$_2$: 1.7%	560 311 29	**This work**
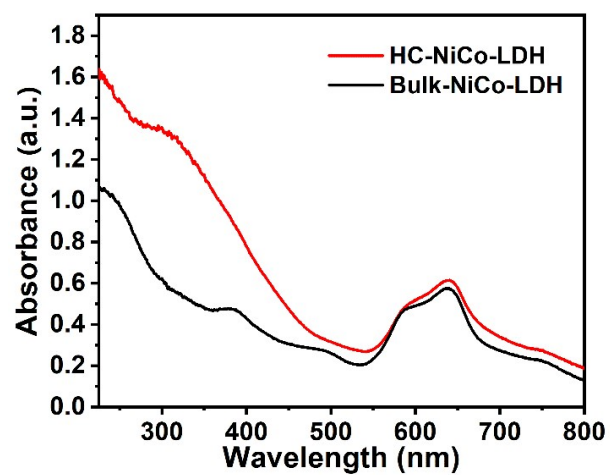
Fig. S19 UV-visible spectra of HC-NiCo-LDH and Bulk-NiCo-LDH.
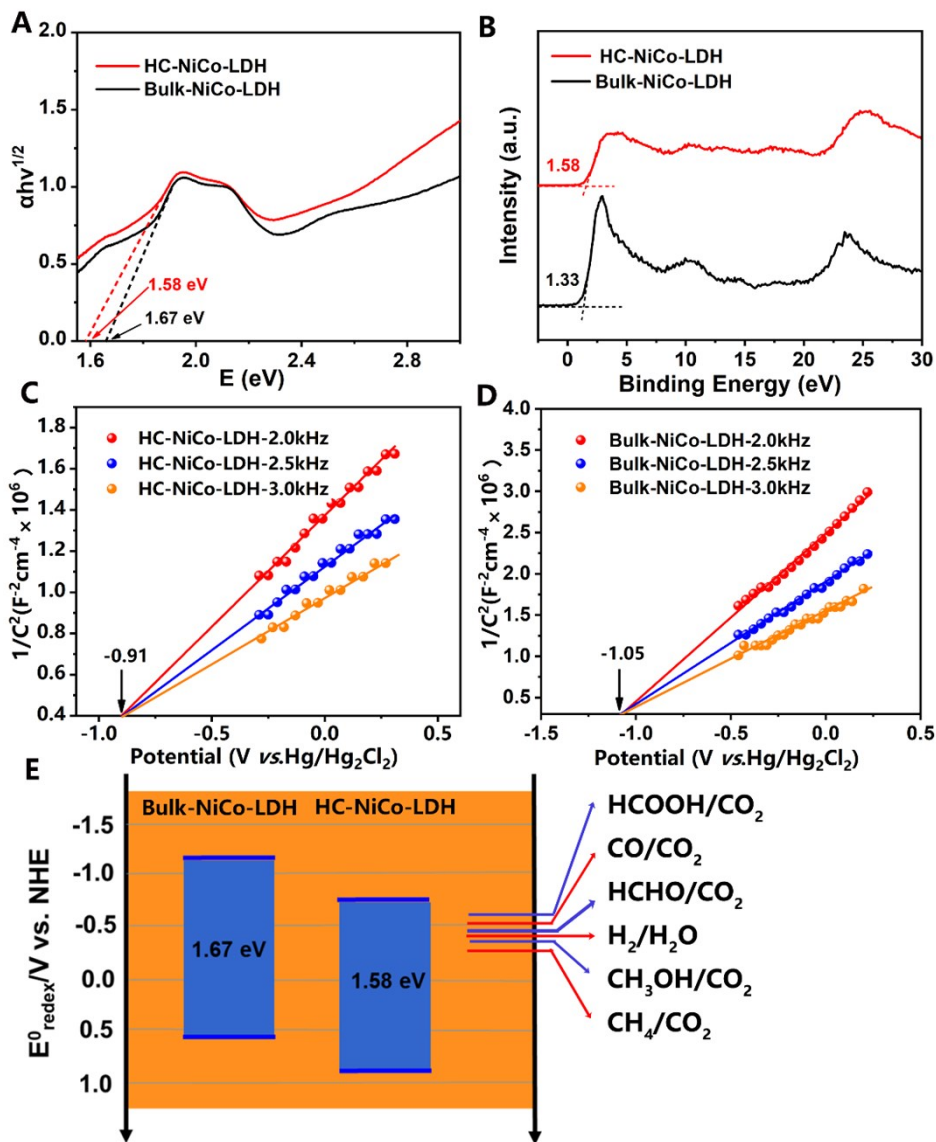
Fig. S20 (A) Tauc plots, (B) valance band XPS spectra, (C, D) and Mott-Schottky plots of HC-NiCo-LDH and Bulk-NiCo-LDH; (E) Conduction band minimum, valence band maximum relative to the CO_2 reduction potentials *vs* NHE at pH 7, and band gap energy of HC-NiCo-LDH and Bulk-NiCo-LDH.

Both HC-NiCo-LDH and Bulk-NiCo-LDH exhibited strong optical absorption with the band gap energy was 1.58 eV, 1.67 eV, respectively, according to the corresponding Tauc plots (Fig. S20 A), close to the theoretical calculating values. These observations affirmed that both HC-NiCo-LDH and Bulk-NiCo-LDH could generate electron-hole pair for photoreduction excited by visible light. Besides, the valency band XPS spectrum was used to ascertain the position of valency band maximum (VBM) relative to the Fermi energy level. The VBM positions of HC-NiCo-LDH and Bulk-NiCo-LDH were estimated to be 1.58 eV and 1.33 eV below the Fermi level (Fig. S20 B). Besides, the flat band potential of HC-NiCo-LDH and Bulk-NiCo-LDH were –0.91 eV, and –1.05 V vs. saturated calomel electrode (SCE) (Fig. S20 C, D), providing the proper redox potentials for CO_2 reduction. Fig. S20 E demonstrated the redox potentials of various products in CO_2 reduction

relative to the normal hydrogen electrode (NHE) at pH 7.
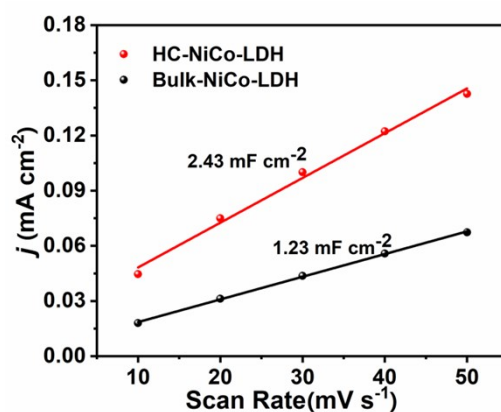
Fig. S21 Charge current density of HC-NiCo-LDH and Bulk-NiCo-LDH-based electrodes plotted against scan rate.
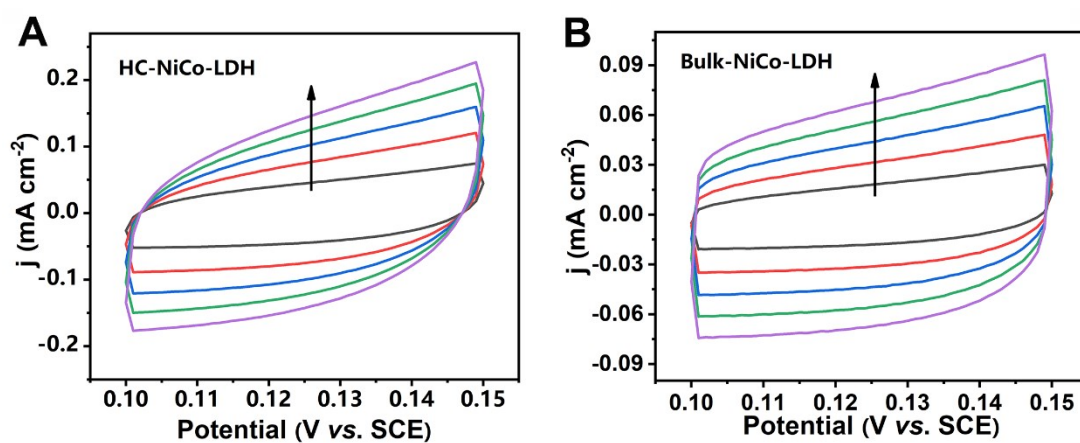
Fig. S22 Cyclic voltammogram tests of HC-NiCo-LDH and Bulk-NiCo-LDH using different scan rates (10, 20, 30, 40, 50mV·s^{-1}, respectively).
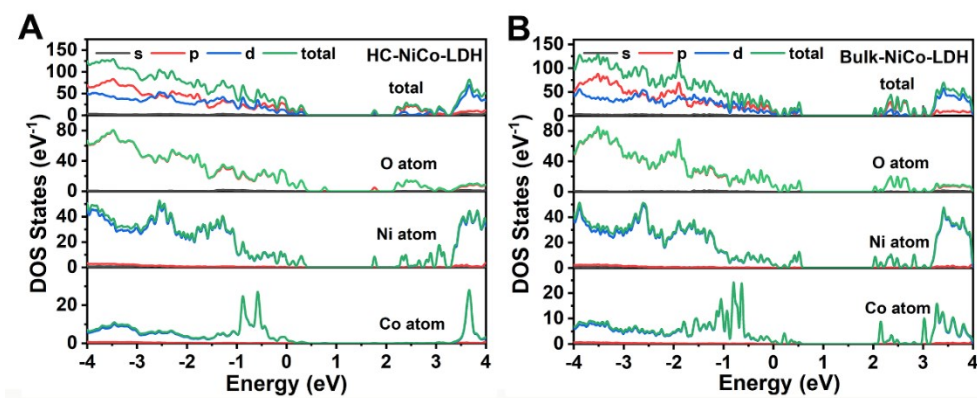
Fig. S23 Total and partial electronic density of states (TDOS and PDOS) for (A) HC-NiCo-LDH and (B) Bulk-NiCo-LDH. The Fermi level was set to zero.
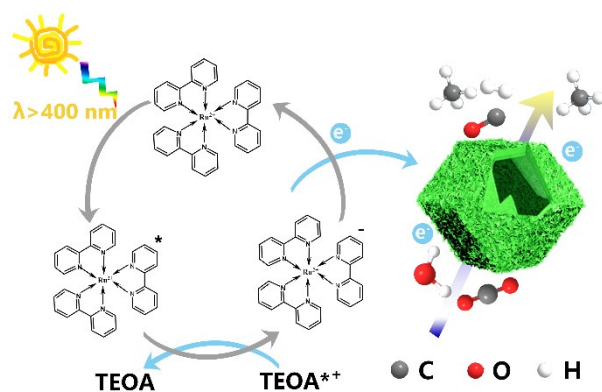
Fig. S24 The mechanism schematic of the photocatalytic CO_2 reduction on HC-NiCo-LDH.

References

1   J. Qin, S. Wang and X. Wang, Visible-light reduction CO_2 with dodecahedral zeolitic imidazolate framework ZIF-67 as an efficient co-catalyst, *Appl. Catal. B-Environ*, 2017, **209**, 476-482.

2   H. Zhang, J. Wei, J. Dong, G. Liu, L. Shi, P. An, G. Zhao, J. Kong, X. Wang and X. Meng, Efficient visible‑light‑driven carbon dioxide reduction by a single‑atom implanted metal–organic framework, *Angew. Chem. Int. Ed.*, 2016, **55**, 14310-14314.

3   Y.-X. Pan, Y. You, S. Xin, Y. Li, G. Fu, Z. Cui, Y.-L. Men, F.-F. Cao, S.-H. Yu and J. B. Goodenough, Photocatalytic CO_2 reduction by carbon-coated indium-oxide nanobelts, *J. Am. Chem. Soc.*, 2017, **139**, 4123-4129.

4   H. Rao, L. C. Schmidt, J. Bonin and M. Robert, Visible-light-driven methane formation from CO_2 with a molecular iron catalyst, *Nature*, 2017, **548**, 74-77.

5   X. Cui, J. Wang, B. Liu, S. Ling, R. Long and Y. Xiong, Turning Au nanoclusters catalytically active for visible-light-driven CO_2 reduction through bridging ligands, *J. Am. Chem. Soc.*, 2018, **140**, 16514-16520.

6   J. Wang, T. Xia, L. Wang, X. Zheng, Z. Qi, C. Gao, J. Zhu, Z. Li, H. Xu and Y. Xiong, Enabling visible-light-driven selective CO_2 reduction by doping quantum dots: Trapping electrons and suppressing H_2 evolution, *Angew. Chem.Int. Ed.*, 2018, **57**, 16447-16451.

7   S.-L. Xie, J. Liu, L.-Z. Dong, S.-L. Li, Y.-Q. Lan and Z.-M. Su, Hetero-metallic active sites coupled with strongly reductive polyoxometalate for selective photocatalytic CO_2-to-CH_4 conversion in water, *Chem. Sci.*, 2019, **10**, 185-190.

8   P. Yang, S. Guo, X. Yu, F. Zhang, B. Yu, H. Zhang, Y. Zhao and Z. Liu, Photocatalytic reduction of carbon dioxide over quinacridone nanoparticles supported on reduced graphene oxide, *Ind. Eng. Chem. Res.*, 2019, **58**, 9636-9643.

9   L. Tan, S.-M. Xu, Z. Wang, Y. Xu, X. Wang, X. Hao, S. Bai, C. Ning, Y. Wang, W. Zhang, Y. K. Jo, S.-J. Hwang, X. Cao, X. Zheng, H. Yan, Y. Zhao, H. Duan and Y.-F. Song, Highly selective photoreduction of CO_2 with suppressing H_2 evolution over monolayer layered double hydroxide under irradiation above 600 nm, *Angew. Chem. Int. Ed.*, 2019, **58**, 11860-11867.